Applied Thermal Engineering 280 (2025) 128375

Contents lists available at ScienceDirect

Applied Thermal Engineering

journal homepage: www.elsevier.com/locate/apthermeng

Research Paper

Thermal field in Monti Sabatini volcanic lithostratigraphic successions☆

L. Colacino [a,*], A.C. Violante [b], R. Trinchieri [b], E. Habib [a]

[a] Dipartimento di Ingegneria Astronautica, Elettrica ed Energetica, Sapienza Università di Roma, via Eudossiana 18, 00184 Roma, Italy
[b] Dipartimento Tecnologie Energetiche e Fonti Rinnovabili, ENEA, Centro Ricerche Casaccia Via Anguillarese 301, 00123 Roma, Italy

ARTICLE INFO

Keywords:
Thermal field analysis
Shallow geothermal system
Geothermal gradient
Volcanic lithostratigraphic successions
Distributed Temperature Sensing (DTS)

ABSTRACT

The actual thermal field of the ground is important for the design of systems that exchange thermal energy with the ground. This paper presents a characterisation of the thermal field and basal geothermal flow within the Sabatini volcanic succession, translating these into boundary conditions, and implementing site-specific monitoring with implications for the broader area. Geothermal flow is evaluated using direct temperature data from a one-year in situ monitoring, rather than relying on indirect or model-based estimates, thus addressing a gap in the literature for shallow volcanic geothermal systems. Heat conduction in the lithostratigraphic successions area is investigated through a Distributed Temperature Sensing system installed in five boreholes of varying depths. Vertical and horizontal thermal gradients are calculated to explore the spatial distribution of ground temperature and the relative contributions of conductive and advective transport. Even though seasonal fluctuations impact only surface layers, deeper layers exhibit a non-uniform temperature field due to lithological heterogeneity and groundwater flow. The geothermal heat flow is predominantly upward-directed, up to 55 m depth, while upper layers show downward or null values, suggesting a dominant influence of groundwater and surface conditions. These findings demonstrate that assuming isothermal lower boundaries is inaccurate in volcanic lithologies and support the use of dynamic, data-driven boundary conditions in geothermal system modelling.

1. Introduction

A detailed understanding of the ground thermal field and backdrop geothermal heat flow of ground is essential for modelling the performance of Borehole Heat Exchangers (BHE) and, more generally, for monitoring low-depth systems which exchange heat with the surrounding ground. Estimation and monitoring of the ground thermal field have been the subject of few studies. Due to the strong site-dependency of these experiments and the mutual correlation between thermal and ground properties, additional data are desirable. Moreover, estimation of deep geothermal heat flow is often unrelated to direct temperature measurements as it mostly relies on existing well logs measurements adopted for the studies.

As reviewed by Hermans *et al.* [1], the more promising temperature measurement techniques for shallow geothermal systems consist of Electrical Resistivity Tomography method (ERT), Self-Potential method (SP) and Distributed Temperature Sensing (DTS).

ERT is an indirect measurement technique, typically associated with an average error ranging from 10 % to 20 % [2], which can lead to temperature uncertainties of at least 1 K in standard ground temperature monitoring scenarios. Meanwhile, the electrodes used in the SP method are temperature-dependent and sensitive to minor thermal variations [3], as commonly encountered in low-enthalpy geothermal applications.

DTS is a class of fiber optic sensors broadly employed in temperature measurement of large structures such as oil and gas wells, tunnels, and pipelines [4]. It provides real-time data collection that could also measure the BHE spatio-temporal dynamics, not capturable by pressure–temperature survey tools [5]. This measurement system was already adopted in previous low-enthalpy geothermal system characterization studies, where the fiber was located inside the U-pipe as the closeness of the fiber with the pipe was a significative parameter: Fuji *et al.* [6] included DTS measurements to validate a non-linear regression used to estimate vertical distribution of ground thermal conductivites, while in the case-study of Acuna *et al.* [7] DTS measurements were used to correct the estimation of the thermal resistance of the probe realized through the Ground Response Test (GRT). Hainar et al. [8] obtained thermal conductivities of different layers thanks to DTS measurements under single and double-U configuration, confirming the latter to be more accurate for TRT. Furthermore, Simon et al. [9] carried out both

☆ This article is part of a special issue entitled: 'Conference ExHFT-10' published in Applied Thermal Engineering.

* Corresponding author.
E-mail address: leonardo.colacino@uniroma1.it (L. Colacino).

https://doi.org/10.1016/j.applthermaleng.2025.128375
Received 18 December 2024; Received in revised form 11 September 2025; Accepted 16 September 2025
Available online 17 September 2025

Nomenclature

Symbols

c	speed of light [m/s]
c_P	specific heat [J/kg K]
L	spatial resolution of the optic fibre cable [m]
p	Pearson correlation coefficient [-]
P_d	probability of the photon of being detected [-]
q_z''	vertical heat flow per unit area [W/sqm]
r	vertical to spatial second thermal derivative normalized ratio
s_2	second-order coefficient of the grade 2 least-squares interpolating polynomial
t	time [s]
t_{n1}	measuring time [s]
T	temperature [K]
v_g	refractive index [-]
x	axial direction [m]
y	longitudinal direction [m]
z	ground depth [m]
ΔL	distance between acquisition points of the optic fibre [m]
Δq“	geothermal heat flow accuracy [mW/m^2]
ΔT	temperature accuracy of the optic fibre [K]

Greek symbols

ε	relative temperature sensitivity of the Raman effect [-]
λ	thermal conductivity [W/m K]
Δλ	thermal conductivity accuracy [W/m K]
ρ	density [kg/m^3]

Sub-index

m	mean value

Abbreviations

BHE	Borehole Heat Exchanger
DTS	Distributed Temperature Sensing
ERT	Electrical Resistivity Tomography
GRT	Ground Response Test
P#	Probe n. #
PZ#	Piezometer n. #
SP	Self-Potential

numerical modelling and laboratory-scale experiments to validate the feasibility of using Active DTS (A-DTS) techniques to quantify the thermal conductivity of porous media and to characterize advective heat transport. Read et al. [10] demonstrated that Distributed Fibre-Optic Temperature Sensing (FO-DTS) enables high-resolution spatio-temporal profiling of heat transport dynamics within fractured rock systems. Tyler et al. [11] used FO-DTS for monitoring heat and mass exchange of groundwater with the ground surface but also well circulation, snow hydrology and soil moisture.

For high enthalpy geothermal applications, however, DTS could face problems: geothermal fluids may include hydrogen which may damage the fiber and distort the optical signal through absorption, resulting in a lack of reliability [12].

Previously, among numerical studies which have characterized the thermal fields of the soil, Fuchs *et al.* [13] employed deep thermal field data to define a 3D numerical crustal temperature model by inverse optimization methodology for the conductive thermal field of the Danish onshore subsurface. Cherubini *et al.* [14] investigated the deep thermal profile of a basin in a North German site and its implications with 3D numerical simulations. Thirdly, Toth *et al.* [15] highlighted how the effects of anisotropy and asymmetry of basin groundwater flows have a critical role in discharge and accumulation patterns when using the ground as an inertial tank.

Measurements and assessments of heat flow in volcanic and geothermal areas are reported in the review paper from Wang and Pang [16] that illustrates the current state of the art of the methods used to target the geothermal resources.

Typically, basal geothermal heat flow is calculated from well log temperatures and Fourier's law. An overview of the geothermal heat flow of Northern Italy was assessed by Pasquale et al. [17] thanks to measurements from exploration oil wells. Heat flow mapping and subsurface isotherms were traced for high-enthalpy Larderello region in Italy. The region is enclosed by a 200 mW/m^2 *iso*-heat flow contour line [18]. Surface heat flow density close to Phlegrean caldera reports undisturbed values around 150 mW/m^2 [19]. A review from Montanari et al. [20] reconstructed the temperature distribution at depth in western Sicily through data acquired via oil and gas exploration data log. Studies for Heat Flow Densities (HFD) are performed in the tectonic provinces crossed by the southern segment of the European Geotraverse by Della Vedova et al. [21], concluding Tyrrhenian area observes values of the order of magnitude of 100 mW/ m^2.

Yet, in many applications, the BHEs are much shallower than the depths tackled in these papers. In addition, the geographical area of the site does not present a baseline study neither regarding the thermal field nor the basal geothermal heat flow.

Thus, despite the growing interest in shallow geothermal systems, few studies have directly monitored the undisturbed thermal field and basal heat flow at depths relevant for BHEs in volcanic lithologies. Most existing work relies on extrapolated or modelled data from deeper wells or unrelated geologies. A research gap persists in the high-resolution characterization of the near-surface geothermal gradient and its implications on heat exchange modelling. This study fills this gap by providing in-situ, year-round DTS monitoring in five boreholes, enabling the assessment of both vertical and lateral thermal gradients and their role in determining accurate boundary conditions for geothermal models.

The heat transfer affecting the volcanic lithostratigraphic succession under analysis is attributed to three primary phenomena: advection from the external environment, lateral advection contingent upon the presence of aquifers, which may result in heat supply or discharge depending on groundwater temperature, and conduction from the underlying strata due to the deep geothermal heat flux.

In this paper, heat flow and temperature evolution over space and time in the ground substrates of a low-enthalpy geothermal system are investigated and monitored over a year through measurements of temperature acquired via Distributed Temperature Sensing technique. By acquiring the data of the thermal field, thanks to the distribution of the optic fibre cable over depth for five wells, it is possible to determine: the vertical and horizontal thermal gradients over the monitoring period, their relevance in the heat conduction phenomena and the basal geothermal heat flow of the low-enthalpy resource up to a depth of 85 m.

The survey relates to volcanic substrates, as a prior investigation [22] documented the presence of the Sabatini volcanic succession in the ground domain utilized for the BHEs field.

2. Method

At the ENEA-Casaccia Research Centre, north of Rome (Italy), a pilot low-enthalpy geothermal system was installed in 2021. Ground temperatures are measured in 5 wells of different depths by using a Distributed Temperature Sensing system. The arrangement of the wells is shown in Fig. 1: each well is 9-metres distant from the adjacent one,

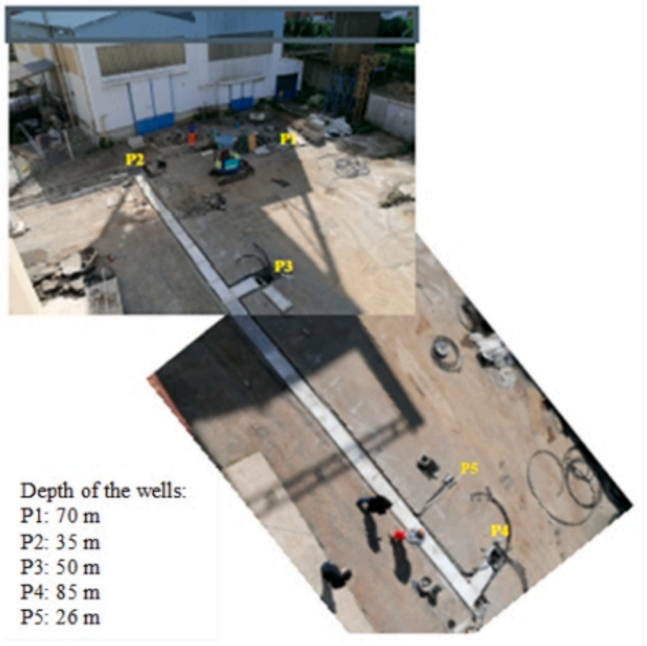

Fig. 1. View from above of the borehole field including the depth of wells.

except P4 and P5, that are 3-metres distant.

The installed optical fiber is a "DiTeSt Ordinary Temperature Sensing cable", manufactured by Smartec SA (Switzerland). The cable has a nylon outer sheath and a steel core. The core tube is hermetically sealed and contains four optical fibers that can be used for measurements, each 9 μm in diameter. They are insensitive to bending, with a double-layer acrylate coating to improve micro-curving performance. The cable offers high resistance to tensile strength, crushing, lateral waterproofing, chemicals, and abrasion.

The cable is installed outside the double U-pipe, as the final aim is to measure the BHE ground temperatures at each depth and the proximity of the fiber with the pipe was not a significative parameter.

The temperature limits of the measuring system are reported in Table 1.

The DTS system acquires measurements of temperature by Raman effect, an inelastic scattering of photons by matters that is used to detect the values of temperature distributed over the entire length of the fiber. Back-scattered light contains three spectral components, among which the intensity of the Anti-Stokes band is temperature dependent. The ratio of the latter to the Stokes component, which is temperature insensitive, provides the local value, as stated in the studies of Ukil *et al.* [23].

Temperature measurements uncertainties increase non-linearly with the length of the fiber. The quantification of the uncertainty through a proper calibration method and a temperature drift correction of the data shows robust results for the current technology as highlighted by Mazzotti *et al.* [24]. DTS provides average values of temperature weighted on sample data acquired every settled measuring time. The performance criteria and standards of accurate Raman DTS measurements are reported by Bolognini and Hartog [25].

Different trade-offs among measuring time (t_{n1}), spatial resolution (L) and temperature accuracy (ΔT) are summarized by Equation (1) firstly proposed by Stierlin *et al.* [26] and subsequently reviewed by Bolognini and Hartog. The required measurement time to achieve the desired temperature resolution is function of the sensing fibre length, the distance between an acquisition point and the successive one (ΔL), equal to 2 m for the current case, the relative temperature sensitivity of the Raman ratio (ε) equal to 0.007 K^{-1}, the refractive index (v_g) equal to 1.5, the probability of a photon of being detected for any probe pulse (P_d) equal to 0.1, and the speed of light (c):

$$t_{n1} = \frac{2\, v_g\, L}{\Delta L\, \Delta T^2\, \varepsilon^2\, P_d\, c} \quad [s] \tag{1}$$

Eq. (1) was reversed to obtain the temperature accuracy of the DTS measurements of the pilot system located at the ENEA Casaccia research centre.

$$\Delta T = \sqrt{\frac{2\, v_g\, L}{\Delta L\, t_{n1}\, \varepsilon^2\, P_d\, c}} \quad [K] \tag{2}$$

As the acquisition time (t_{n1}) was set to 15 min, each well, depending on its total length (L), consisting of both the vertical and the horizontal section, connecting the well-head with the acquisition PC, will be characterized by a different sensitivity of measure. Note that the horizontal section of P2 cable, which is the nearest well to the acquisition PC, is 10 m long. Temperature measurements are taken only over vertical depth. Results of temperature accuracy in function of the total lengths are collected in Table 2, where L, as previously stated, consists of both the vertical and horizontal length of the optic fibre cable.

Soil stratification was determined from the excavated material during the construction of the wells. The thermophysical properties were measured on rock samples: thermal conductivity, thermal resistance, and the undisturbed temperature of the ground, have been extrapolated by the thermal profiles of the probes obtained after the Ground Response Test. Subsequently, the data were corrected through measurements on rock core samples from the stratigraphy, executed with a conductivity meter. According to its technical specifications, the instrument has an uncertainty of 5 %. This allowed for the creation of a detailed specific lithostratigraphic sequence for each well, enabling the determination of the thickness of each lithotype, the changes, and heteropies of facies in each layer. Fig. 2 shows the reconstruction of the stratigraphy on the vertical plane from P2 to P4.

Table 3 reports the thermos-physical properties of the specific lithostratigraphic succession for well P4.

GRT results order of magnitude is coherent with precedent studies dealing with ground thermal conductivity estimation in presence of sandy loam, as shown by the studies of Urresta *et al.* [28] and clay lithologies, as reported by the studies of Busby [29] on different soil types in Great Britain, where associated thermal conductivities were estimated using soil texture data from the "BGS Parent Material Map".

The heat flux rate is calculated as a purely conductive field. Each layer is assumed to be isotropic. The impact of groundwater flow is neglected..

According to the previous hypothesis, Equation (3) is used for calculating the vertical heat flux per unit area (q''_z) in function of the thermal conductivity of the specific lithology ($\lambda_{(\Delta z)}$), the temperature (T) and the ground depth (z). In addition, the method chosen for the calculation of the heat flow matches the method adopted by the

Table 1
Technical temperature limits for DiTeSt.

	Lower limit (K)	Upper limit (K)
Installation temperature	263.15	323.15
Operating temperature	233.15	358.15
Short-term temperature (max 1 h)	223.15	423.15

Table 2
Temperature accuracy of DTS measurements for each well.

	Well P1	Well P2	Well P3	Well P4	Well P5
Depth (m)	70	35	50	85	26
Horizontal distance from acquisition unit (m)	19	10	19	31	28
Total length (m)	89	45	69	126	54
ΔT (K)	0.095	0.048	0.073	0.124	0.057

Fig. 2. Lithostratigraphic sequence over depth on the vertical plane from P2 to P4 [27].

Table 3
Thermal conductivities of the lithostratigraphic succession for well P4.

Material	Thermal conductivity (W/ m K)	Depth (m)	Thickness (m)
Ignimbrite	1.02	0.00 – 3.00	3.00
Brown tuff	0.93	6.00	3.00
Incorporated lithics tuff	0.89	7.50	1.50
Fine-grained tuff	0.83	10.00	2.50
Clear sandy tuff	0.87	11.00	1.00
Grey slag tuff	0.86	15.00	4.00
Pyroclastic clayey material	0.81	17.50	2.50
Clay tuff	0.87	19.00	1.50
Variable-grained tuff with heterogenic lithics	1.01	22.00	3.00
Lava	1.48	33.50	11.50
Earthy tuff	0.79	34.50	1.00
Sandy pozzolana	0.90	36.50	2.00
Greenish pozzolana	1.07	38.50	2.00
Ochre tuff	0.98	46.50	8.00
Reddish-brown tuff	0.93	52.00	5.50
Black slag red tuff	1.00	65.50	13.50
Sandy loam tuff	0.66	69.00	3.50
Avana tuff	0.78	82.00	13.00
Sacrofano tuff	0.89	86.00	4.00
Sandy silt	1.06	94.00	8.00

International Heat Flow Commission [30] in the determination of the Global Heat Flow Database. The convention used for the sign of the heat flow is positive in the direction of the superficial surface, i.e. opposite to gravity force, whilst the z axis is directed downward.

$$q_z'' = -\lambda_{(\Delta z)} \frac{(T_z - T_{(z+\Delta z)})}{\Delta z} \left[\frac{W}{m^2}\right] \tag{3}$$

The relative uncertainty of the vertical heat flow is calculated as the root-sum-square of the relative uncertainty of the thermal conductivity and the propagated uncertainty of the temperature difference, as shown in Eq. (4):

$$\frac{\Delta q''}{q''} = \sqrt{\left(\frac{\Delta\lambda}{\lambda}\right)^2 + \left(\frac{\Delta T_m \sqrt{2\,(1-p)}}{(T_z - T_{(z+\Delta z)})_m}\right)^2} \; [\%] \tag{4}$$

The average uncertainty value for the temperature measurement is taken from Table 2 for well P4, which is the one used for heat flux calculations, equal to 0.124 K. The relative uncertainty of the conductivity meter, as previously mentioned, is 5 %. Since the temperature difference along the vertical axis (z-axis) is measured by the same optical fibre, its associated uncertainty is correlated. The effect of this correlation is accounted for using the Pearson correlation coefficient [31], which quantifies the linear relationship between two datasets. In this case, the coefficient p is 0.99. The average vertical temperature difference in the field, measured every 2 m, is 0.29 K. Consequently, the relative error in the vertical heat flux calculation is 6.85 %.

Within the aforementioned hypotheses the temperature field is described by Fourier's law.

$$\nabla^2 T = \frac{\rho\, c_P}{\lambda} \frac{\partial T}{\partial t} \left[\frac{K}{m^2}\right] \tag{5}$$

Where Laplace's operator, in cartesian coordinates, is the sum of the second derivatives along each axis.

$$\nabla^2 T = \frac{\partial^2 T}{\partial x^2} + \frac{\partial^2 T}{\partial y^2} + \frac{\partial^2 T}{\partial z^2} \left[\frac{K}{m^2}\right] \tag{6}$$

The z-axis is parallel to gravity downward oriented, corresponding to the depth. The x-axis is along the line where P2, P3, P4 and P5 are aligned, while the y-axis is orthogonal to x and y, aligned to the line from P1 to P2.

According to Eq. (5), the time evolution of the temperature is proportional to Laplace's operator. The DTS provides enough temperature values for the calculation of the third addendum on RHS of Eq. (6). Yet, using data from the different wells it is possible to calculate the second derivatives of the temperature field along x-axis. Considering its limited accuracy due to the scarcity of measurement points, it is useful to establish its magnitude, whether negligible or significant, compared to the vertical second derivatives of the temperature field. This calculation is therefore intended to refute the hypothesis that any anomalies in the geothermal heat flux estimation are significantly influenced by horizontal temperature gradients and thereby also validate the use of Eq. (3) for the current case.

The second derivative is calculated by applying the Ordinary Least Squares (OLS) method to the temperature measurements matrix. Eq. (7) shows the relation between the second derivative and the second-order

coefficient of the grade 2 least-squares interpolating polynomial (s_2).

$$\frac{d^2T}{dx^2} = 2\,s_2\left[\frac{K}{m^2}\right] \tag{7}$$

The installation near the BHE system of two piezometers (PZ1 and PZ2), 100 m apart, has made possible to quantify the basic hydrological and thermal properties of the aquifer. Measures acquired through piezometers are reported in Table 4.

The hydraulic load is calculated from the hydraulic head difference between the two piezometers. The groundwater temperature is 17.50 °C, in agreement with the results for adjacent aquifers reported by Taviani et al. [32].The measured value of hydraulic gradient, equal to 9 mm/100 m, indicates the presence of the regional aquifer of lake Bracciano, which intersects both the piezometers and the geothermal wells perpendicularly and influences the groundwater flow regime in the Sabatini volcanic area. Consequently, the aquifer's contribution to heat exchange within the ground domain is mainly horizontal, orthogonal to the probes.

During the drilling of the geothermal field, the groundwater level was first encountered at the base of the lava flows and later stabilized within the lava unit itself, at a depth of approximately 26 m. This observation is consistent with measurements from the piezometers and reflects the high permeability and fracturing of the lava formations, which allow for significant groundwater flow. These hydrogeological conditions support the presence of horizontal flow across the wells.

The current analysis focuses on the evolution of the undisturbed thermal field during the period following the installation of the geothermal probes (from 1st May 2021 to 30th April 2022), when the borehole field was still inoperative. Data start from two weeks after the end of the Ground Response Test (GRT), that was done to measure the thermal properties of the ground along each probe. The Ground Response Test has been performed exclusively on well P1, so the other probes had experienced no thermal perturbation after the completion of their casings.

3. Results and discussion

Continuous monitoring with DTS allows analysis of the evolution of the thermal field over time and depth. The components of Eq. (6) are analysed to determine the preferential direction of the thermal gradient. Once through Eq. (7) the vertical gradient is verified to be dominant over the horizontal contribution, through Eq. (4) the basal geothermal heat flow has been evaluated.

Figs. 3 to 10 show the evolution of the thermal field at different depths, from 2 to 85 m depth.

At 2 m depth there is a seasonal temperature variation of the layer of almost 30 degrees. The temperature evolution is homogeneous for all wells. These values are compared with the climate data of the research centre ENEA Casaccia for year 2021 [33]. The maximal external air temperature is 38 °C and the minimal is −1 °C. However, Fig. 3 displays the daily averages of the external air. The difference between ground and air temperature is larger during summer, close to 10 K, while it is smaller during winter, approximately 2 K, due to the contribution of solar heating to surface temperature.

Fig. 4 shows how surface heat transfer becomes less relevant with the increase of depth. Even though one probe, P3, is more strongly influenced by external conditions. This peculiarity is due to the wider concrete cylinder of the surface section of the well (due to a collapse occurred during well construction phase).

Table 4
Measurements of piezometers.

Piezometer	Hydraulic head (m)	Distance with PZ1 (m)	Temperature (°C)
PZ1	25.30	–	17.50
PZ2	26.20	100	17.50

From Figs. 4–6, all probes show a temperature decrease during the observation period, at almost any depth, while the steepness of the decrease is quite variable. Most time series show a decrease of 0.5 K in 200 days, while P4 at 18 m and P3 at 24 m have a 1 K decrease in 50 days. As these two values correspond to permeable surface layers, this phenomenon is attributable to advection due to groundwater flow in a non-horizontal layer with heat transfer mainly due to conduction to the other layers.

At 30 m depth, in proximity to the end of the lava layer, the strongest impact of the groundwater flow on the thermal field is observed. This result agrees with the results of the previously exposed piezometers. In fact, comparing Fig. 6 and Fig. 7, a significant variation is experienced by all wells in a 6-metres depth difference. Particularly, well P3 and P4 see a decrease of more than 0.5 K from 24 to 30 m in depth. In addition, the spatial gradient between the different wells flattens out.

By observing Figs. 5–8, it is evident that the temperature differential between well P1 and P4 decreases as the depth of measurement increases, from more than 1 K at 18 m depth to less than 0.25 K at 50 m depth. This demonstrates that while thermo-stratigraphic properties play a role in shaping the transient evolution of the thermal field, the influence of the background geothermal heat flow becomes more significant at greater depths, as also verified by the groundwater table estimated with piezometers.

At the beginning of the measurements at 50 m depth, well P1 has a greater temperature due to the Ground Response Test. Its effects become irrelevant after at least 150 days from the beginning of the monitoring period.

Figs. 8 and 9 exhibit similar temperature profiles evolution for well P1 and P4, with different average values. Finally, observing Fig. 9and Fig. 10, the intensification of the basal geothermal heat flow is evident with a global increase of temperature field of almost 1 K between 69 m depth and 85 m depth.

Moreover, time evolution of the temperature at the deepest measure point, which is shown in Fig. 10, at the depth of 85 m, over a 1-year time period shows unexpected fluctuations. These may be due to fluctuations in the upwellings of hydrothermal fluids from the bottom, even though the maximum variations are only slightly above the measurement precision.

The recorded thermal field indicates that the deep geothermal heat flow is non-constant due to fluctuations that may be due to hydrothermal hot spots. Hence, assuming the background as an isothermal basal surface is inaccurate. Therefore, it is necessary to investigate the dynamic changes in deep geothermal heat flow to determine its magnitude and estimated value over the specified 1-year period.

Figs. 11 to 13 show the temperature profiles along each probe at the first, at half campaign, and at the last day of considered data.

The overall temperature of wells P1 and P2 is lower than the others. The spatial gradient is due to both the different thermos-physical properties of the lithostratigraphic succession, reported in Fig. 2 and the influence of groundwater flow, which permeates differently the stratigraphy due to the natural spatial anisotropy of lithofacies.

The vertical gradient regularizes in the underlying layers. This is compatible with the presence of an aquifer, as verified by measurements of the piezometers. The deepest layer, in correspondence of well P4, consisting of sandy silt, presents higher temperatures at the bottom, as it is near the bed of the aquifer composed of clays where it is affected by the deep ground geothermal heat flux.

Comparison of data from different wells reveals a horizontal temperature gradient at depths where there are no surface effects. This implies that the lithologies are not perfectly horizontal, as illustrated in Fig. 2, evidencing the significant impact of the different thermophysical properties of the material on the heat transfer [27].

To highlight whether the horizontal heat transfer is relevant, the ratio of the vertical to the spatial second thermal derivative is calculated, these are the third and the first addends in Eq. (6). To ease the detection, the hyperbolic tangent of the ratio is calculated Equation (8):

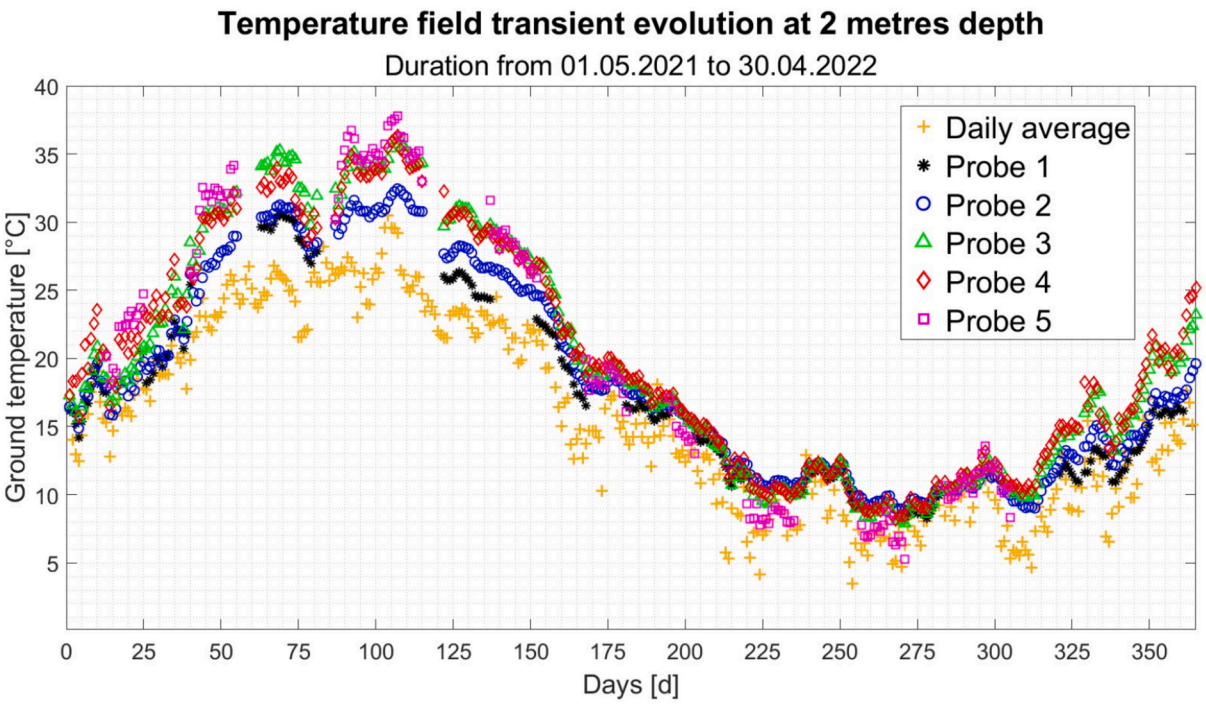

Fig. 3. Temperature evolution in well P1, P2, P3, P4, P5 and air temperature at 2 m depth.

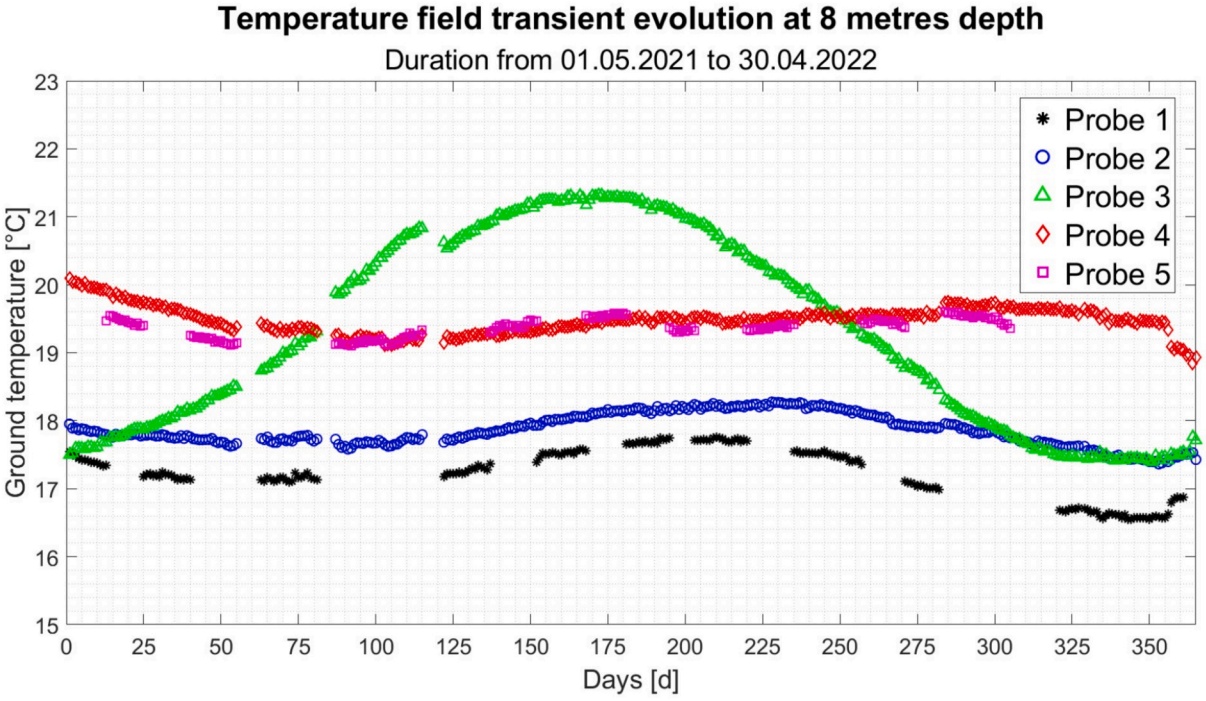

Fig. 4. Temperature evolution in well P1, P2, P3, P4, and P5 at 8 m depth.

a value close to 1 implies the vertical second thermal derivative is of a higher order of magnitude, a value close to 0 implies the two components of the gradient are comparable.

$$r = \tanh\left(\frac{d^2T}{dz^2} \Big/ \frac{d^2T}{dx^2}\right) \tag{8}$$

Fig. 14 shows the results of the 3D plot of r in function of ground depth and time (in the period between 1st and 22th August 2021). The vertical second thermal derivative is always the dominant term, with the exception of two specific depths (8 and 18 m): in these layers the second derivative along vertical direction of the temperature field changes sign, as observable in Fig. 11, so a value of r close to zero is expected at those depths. Thereby, the hypothesis of dominant vertical thermal gradient is verified. This confirms that Eq. (5) and Eq. (6) could be simplified to the more immediate Eq. (3), without introducing simplifications for the study of the present physical phenomenon.

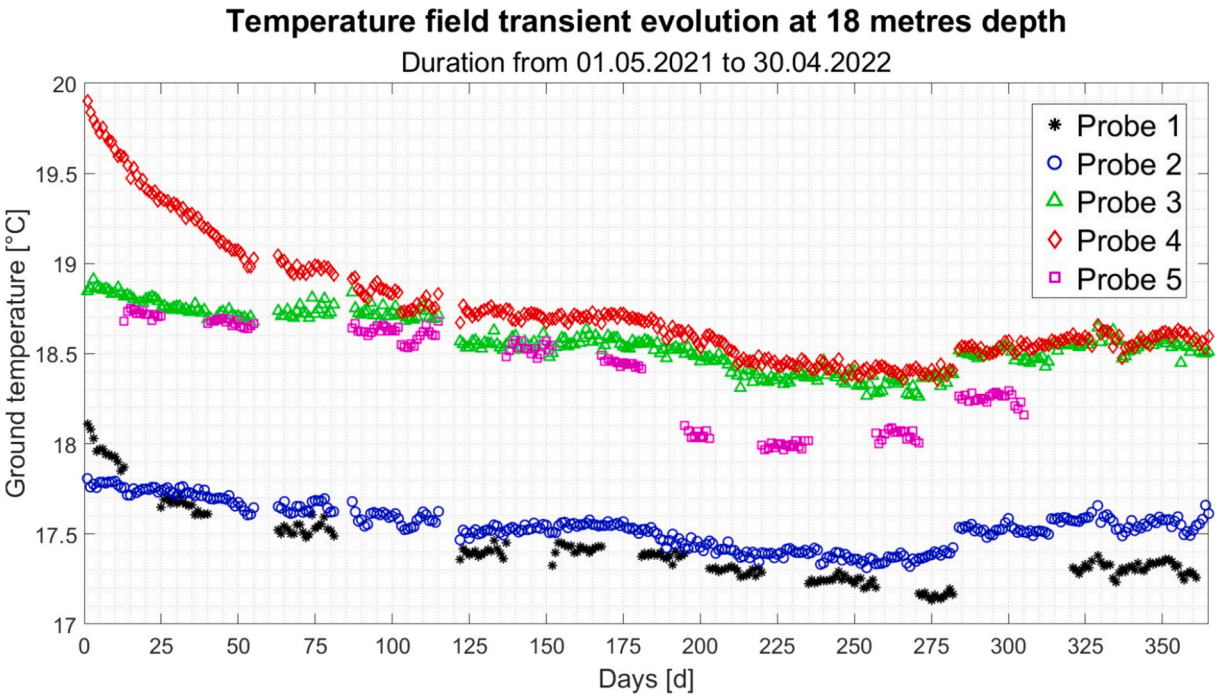

Fig. 5. Temperature evolution in well P1, P2, P3, P4, and P5 at 18 m depth.

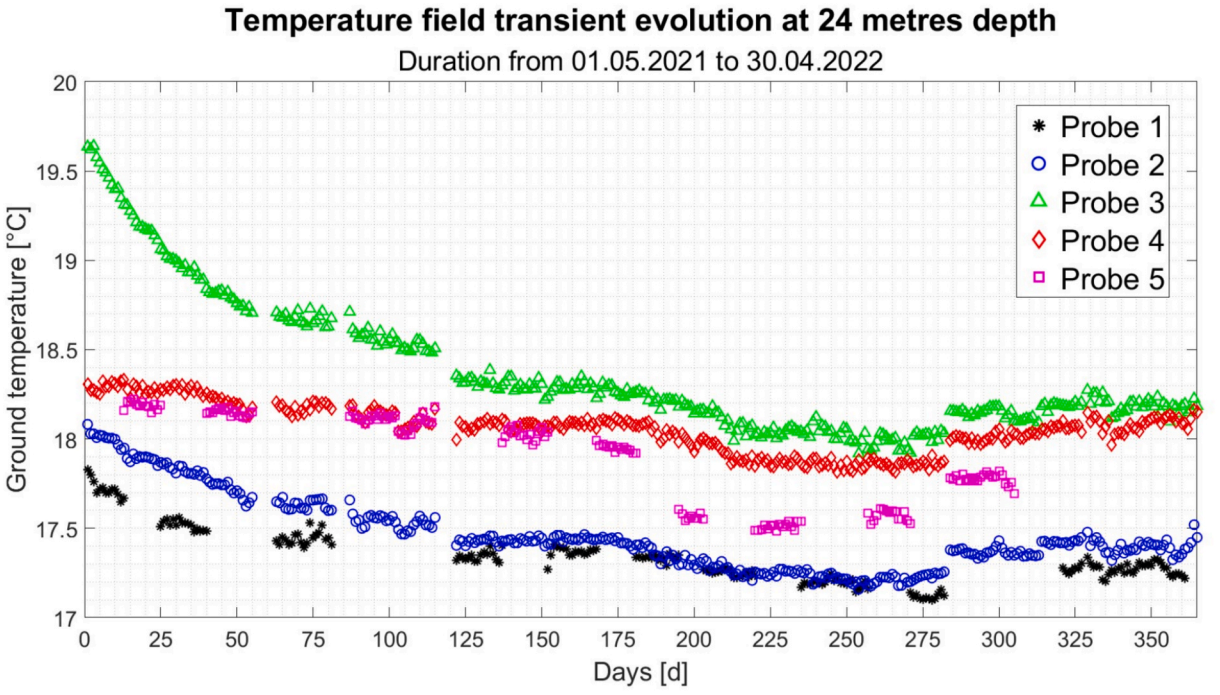

Fig. 6. Temperature evolution in well P1, P2, P3, P4, and P5 at 24 m depth.

With the latter equation, the vertical heat flow of well P4 is evaluated and reported in Fig. 15. Results are reported from 20 to 90 m because above these depths the heat exchange is off the scale as it is mainly dominated by the surface heat flow.

The distribution of heat flux rate shown in Fig. 15 suggests that a basal geothermal flux has an influence between 50 and 85 m depth, then it tends to be null. The upper layers, on the other hand, are significantly influenced by the activity of the aquifer, which releases the thermal energy trapped in the ground.

The accuracy of the measurements is 6.85 %, previously calculated with Eq. (4), and this is backed by the low deviations of values from the trend lines appreciable in Figs. 16–18. In addition, distinct layers exhibit varying heat flux responses, allowing for an appreciation of chronological changes in thermal response.

The enhancement of the heat flow with depth can be appreciated in Fig. 16 and Fig. 17. Indeed, between 75 and 79 m depth the geothermal specific heat flow rate is constant between 20 and 40 mW/m^2, while towards 85 m depth it fluctuates between 80 and 100 mW/m^2. The greater proximity to the aquifer and its horizontal heat dissipation justifies a lower flow for the shallower layers.

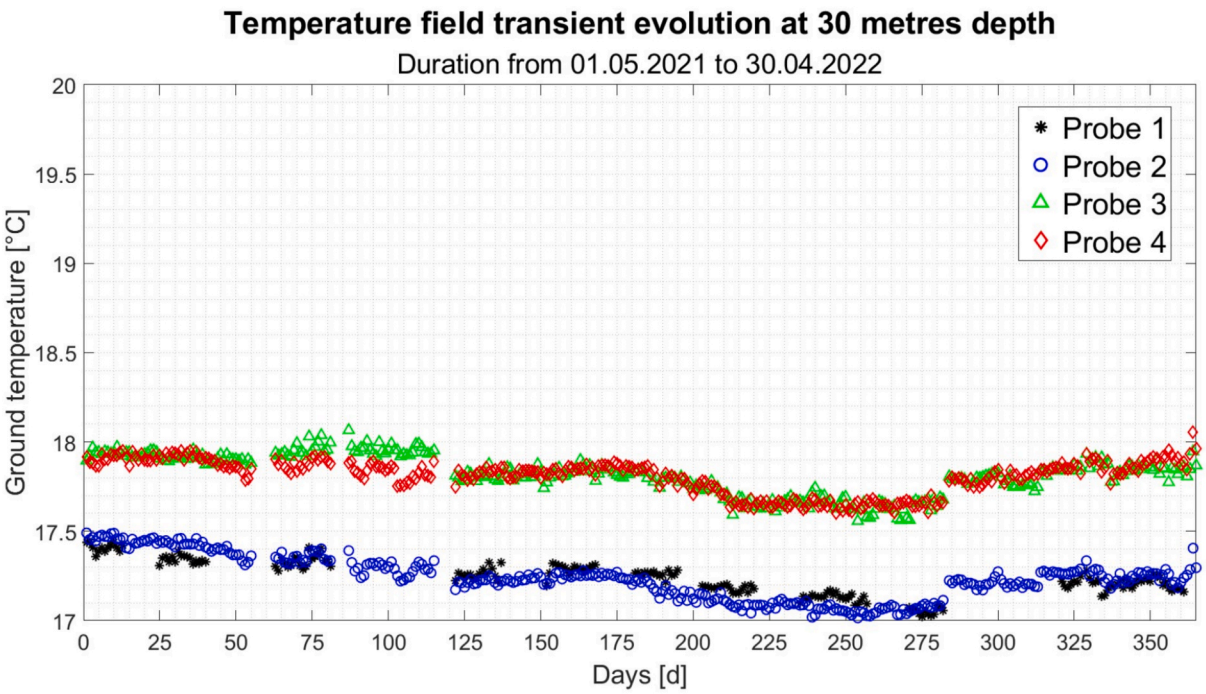

Fig. 7. Temperature evolution in well P1, P2, P3, and P4 at 30 m depth.

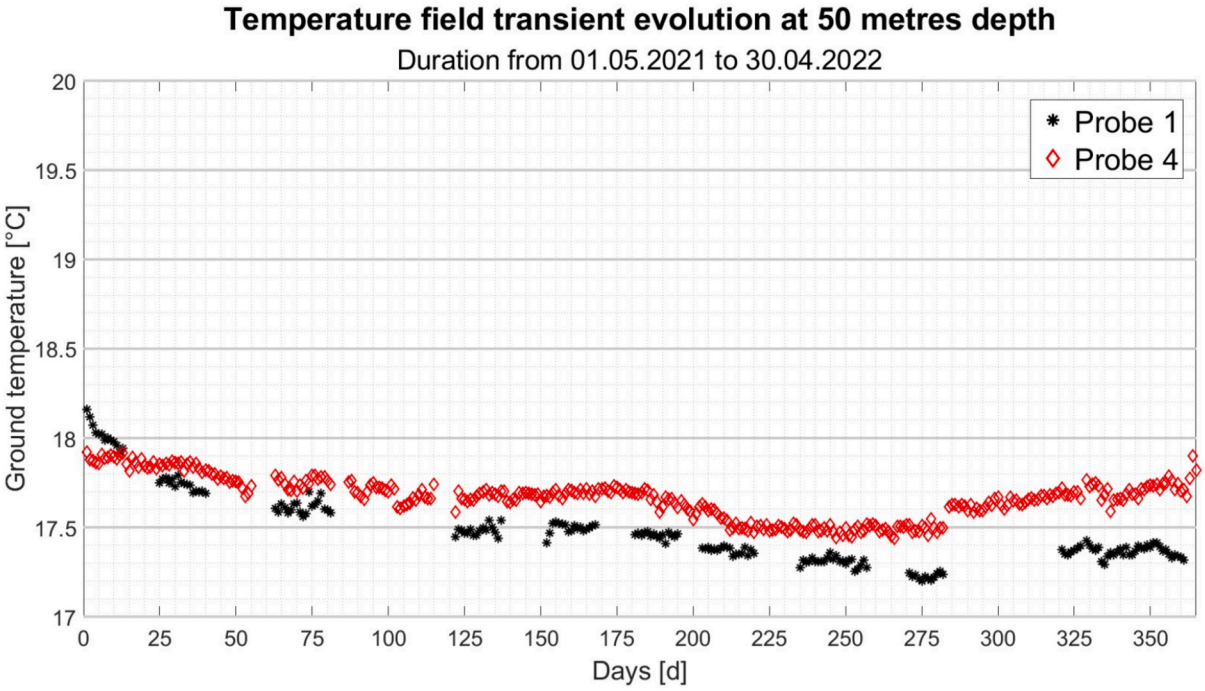

Fig. 8. Temperature evolution in well P1 and P4 at 50 m depth.

Increasing heat flow rates identified below 50 m depth agrees with previous results as the one from Fuchs *et al.* [34], regarding the terrestrial heat flow in Germany, and Verdoya *et al.* [35,36], who analysed the center and northern Apennines in Italy. The latter states for Tyrrhenian domain of ground a median specific heat flow rate of 75 mW/m^2.

While the order of magnitude corresponds, the difference of the specific values between the current case and the literature references is addressed to both the different depth of the present measurement system and the different lithologies respect to the reference case.

Moreover, the entity of the basal geothermal heat flow detected at 85 m matches with the estimation of Pauselli *et al.* [37], which divided the heat flow intensity of middle Italy in two areas, with the western side characterized by high and spatially inhomogeneous heat flows.

Eventually, both Fig. 16 and Fig. 17 show slight decreases and increases of the specific heat flow rate suggesting a yearly variability: a cause may be the influence of the production of the neighboring aquifers, influenced by many factors (for example yearly rainfall) as reported by Ratouis *et al.* [38], as well as the presence of hydrothermal vents, already found in the field.

Heat fluxes are positive upward-directed up to a depth of 55 m, while

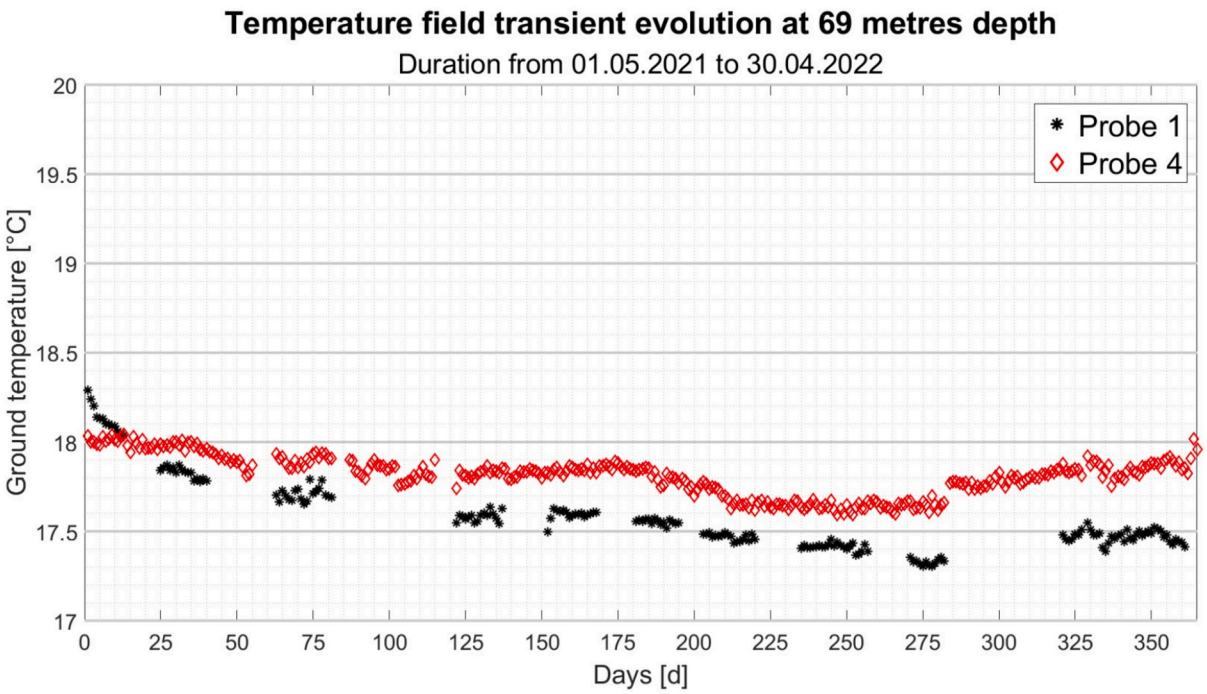

Fig. 9. Temperature evolution in well P1 and P4 at 69 m depth.

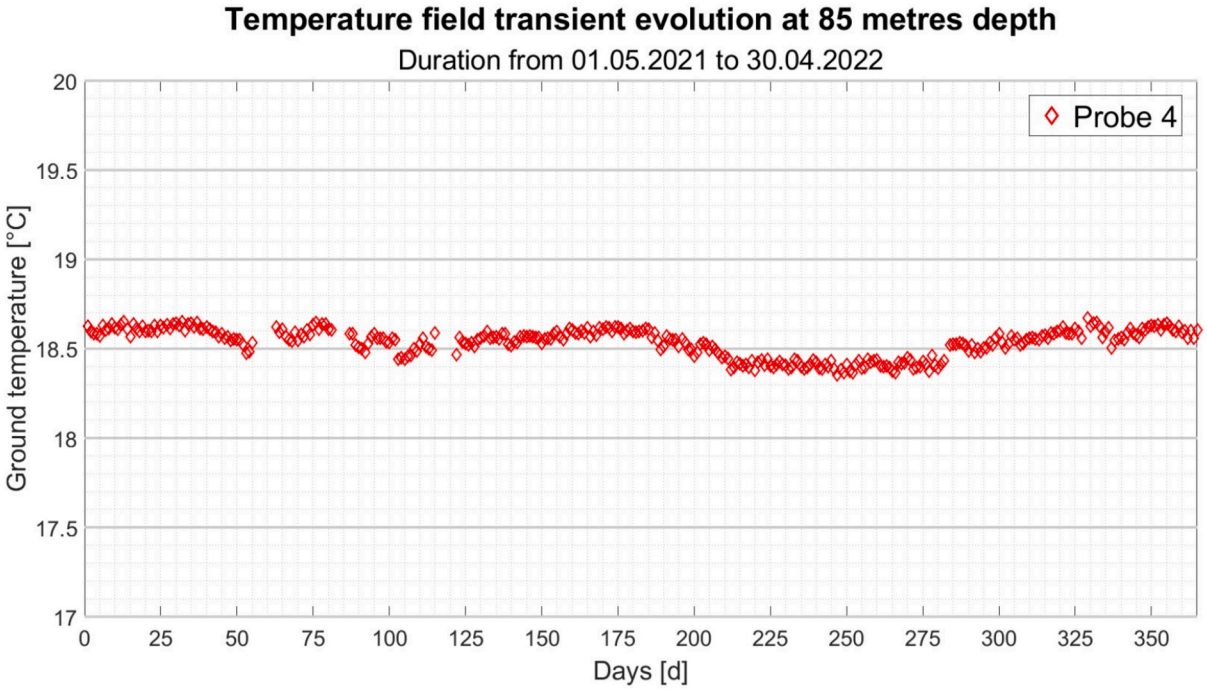

Fig. 10. Temperature evolution in well P4 at 85 m depth.

upper layers show negative or null values, implying the magnitude of the basal heat flux becomes less significant compared to other heat exchange phenomena such as groundwater flow advection and heat exchange with the external environment.

Della Vedova *et al.* [21–39] pointed out the heat flow distribution in the Tyrrhenian area, comprehensive of Latium, reflects a background heat transfer controlled by advection-processes. The results presented in Figs. 16–18 are also in agreement with the heat flow values provided by the Geothopica database for the Tyrrhenian region [40]. The temperature distribution in the shallow layer is greatly affected by processes occurring near the crustal surface. For this reason, the determination of the boundary conditions of ground domain models is more consistent if the backdrop heat flow is calculated.

The effect of an aquifer is appreciable in Fig. 18, where the different lithologies, according to different degrees of fracturing, experience differently the energy balance between the upcoming geothermal heat flow and the transversal groundwater heat flow discharge. Positive vertical heat flow means that the basal geothermal heat flow is still dominant, while negative vertical heat flow implies that groundwater flow removes more heat than comes from the basal surface. The

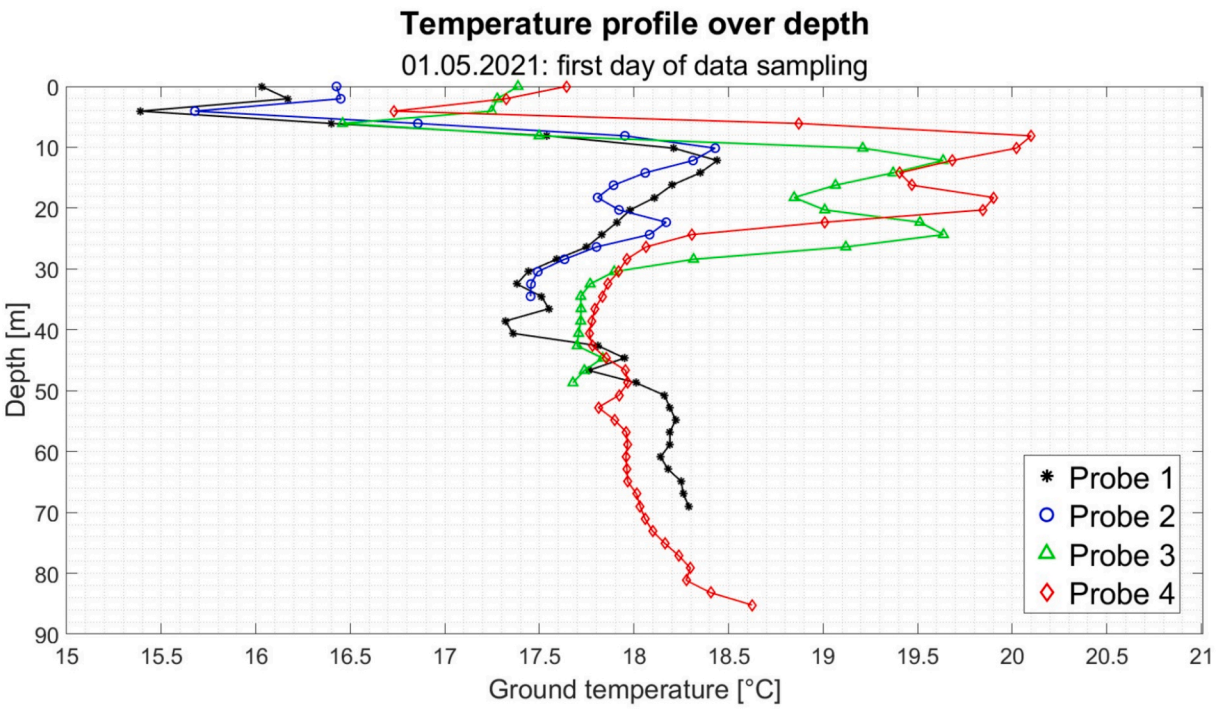

Fig. 11. Temperature profiles along 4 wells in function of depth on the first day of data sampling.

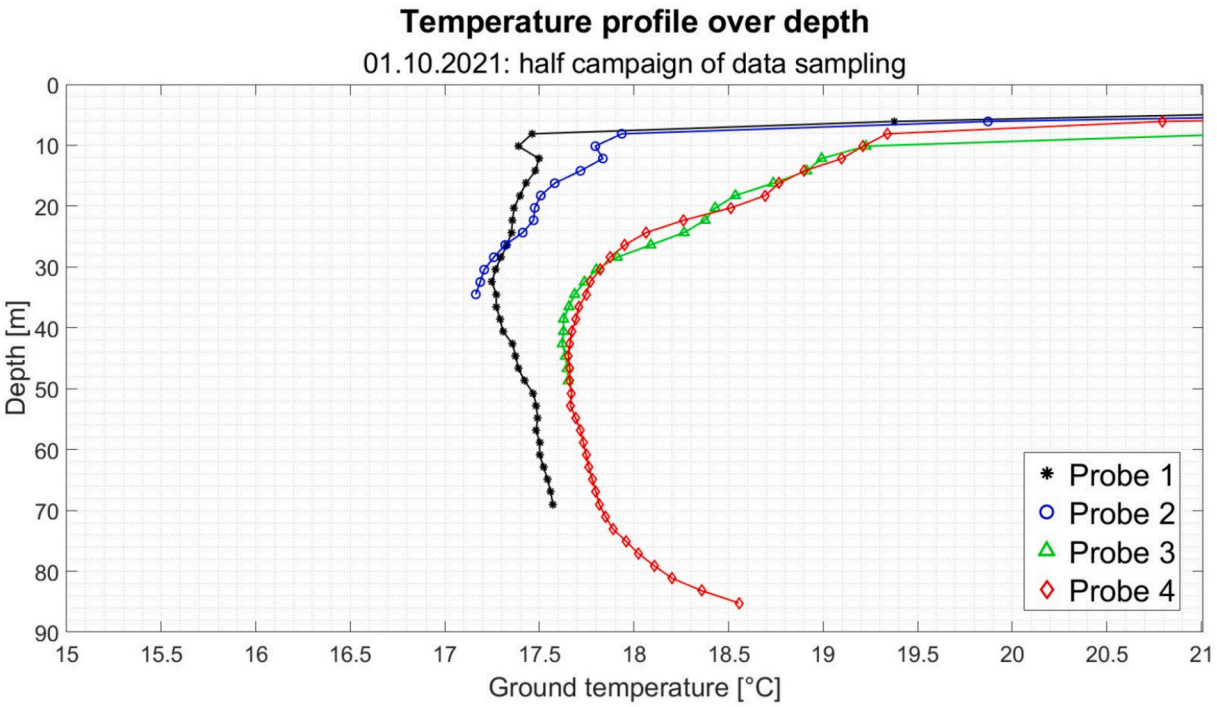

Fig. 12. Temperature along 4 wells in function of depth at half campaign of data sampling.

phenomenon is not constant over time, in accordance with the trend of the aquifer, of which the flow is a function of several variables, including seasonal rainfall.

The heat flow evaluation of Figs. 15-18 confirms estimates of previous studies in the literature and validates them, as the current calculation is based on DTS and GRT measurements while previous studies defined Geothermal Heat Flow maps from temperature measurements from deeper wells.

4. Conclusions

The analysis of both temperature and heat flow along the deepest probe, P4, leads to the conclusion that the baseline bottom surface should be considered at constant heat flow due to observed fluctuations: in fact, the temperature in the Sabatini volcanic lithostratigraphic successions is far from being constant and uniform even at depths where the influence of surface heat transfer is not relevant.

Continuous, high-resolution, DTS measurements are integrated in a

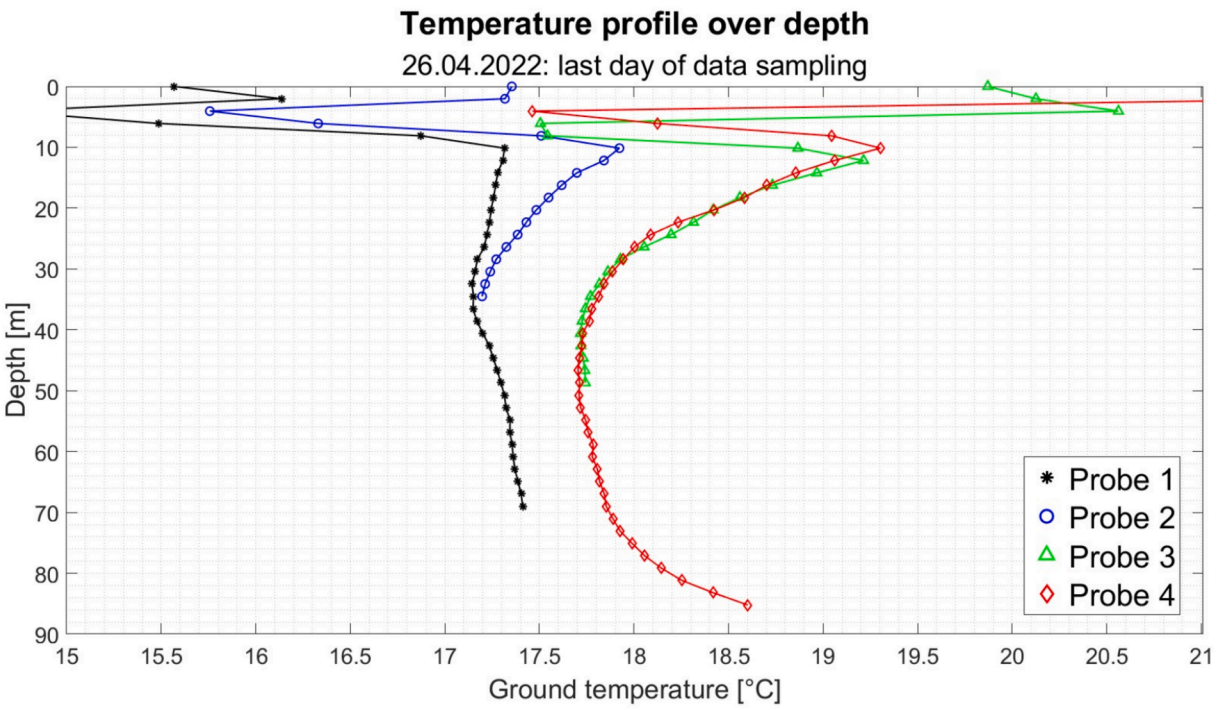

Fig. 13. Temperature along 4 wells in function of depth at half campaign of data sampling.

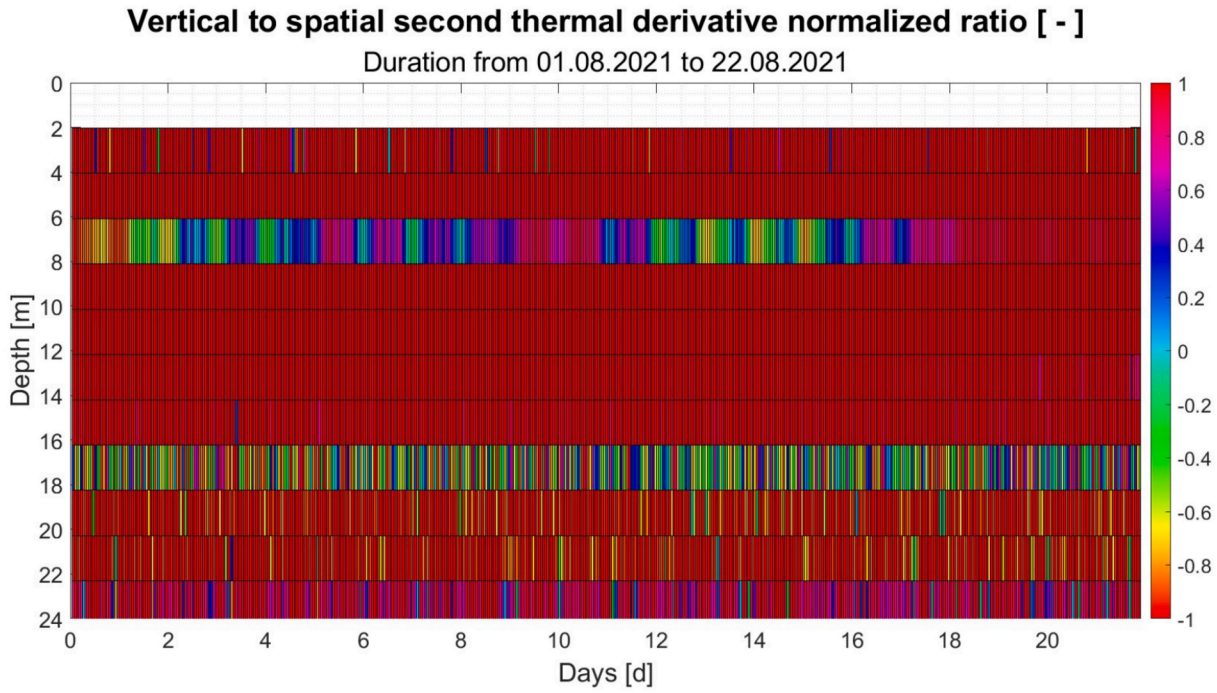

Fig. 14. Vertical to spatial second thermal derivative normalized ratio over depth and time.

multi-well volcanic context to characterize the shallow geothermal field over time. It highlights the limits of static, isothermal boundary assumptions and provides a novel, data-driven approach to inform more accurate geothermal system modelling. Groundwater flow and lithological heterogeneity have major influence on the thermal field. Thus, significant discrepancies should be expected between analytical evaluation of BHEs and their actual performance.

The thermal field analysis executed at the ENEA Casaccia site confirms that Tyrrhenian regions report strong anomalies of undisturbed conductive heat flow greater than 100 mW/m^2, with Latium and the central-southern Tyrrhenian Sea showing wide areas with heat flow values in excess of 200–250 mW/m^2. The results could be helpful for estimating the geothermal potential of the areas within the 'Cesano geothermal field', whose lithotypes belong to the Monti Sabatini volcanic province. This estimate also verifies the previous heat flow mapping of larger regions previously made with less specific data.

Nonetheless, temperature gradients along the vertical axis are much more relevant than those in a horizontal plane. Therefore, even if the

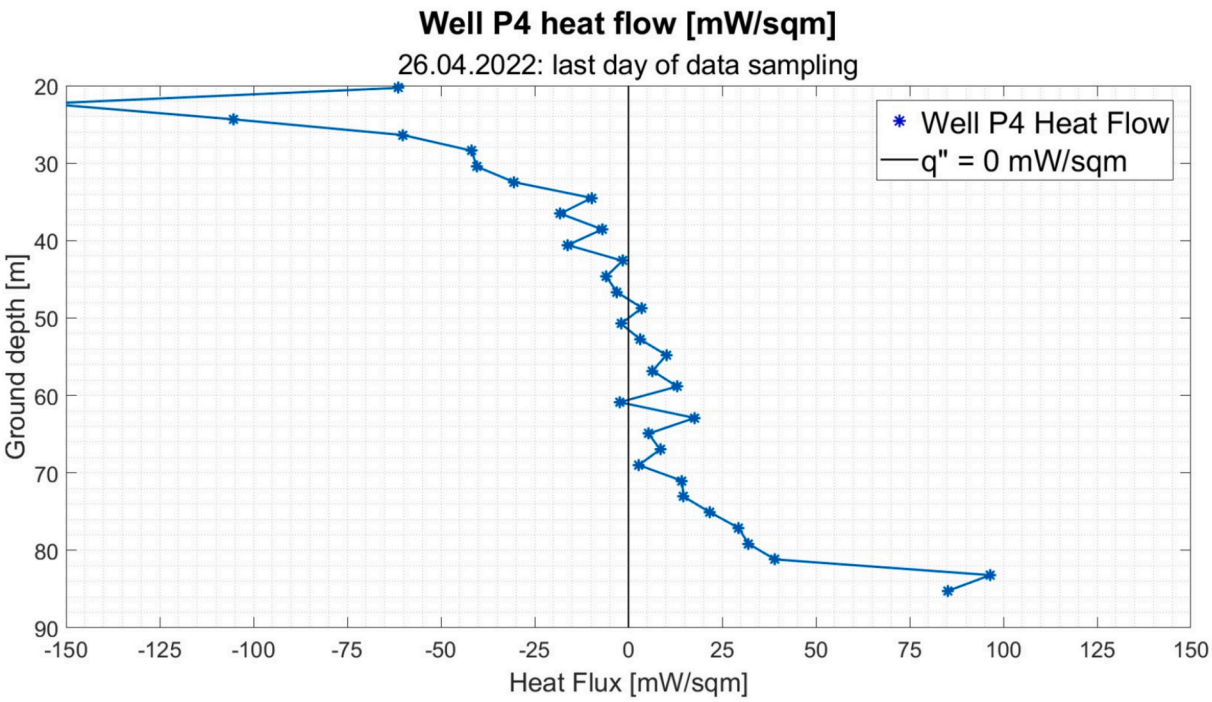

Fig. 15. Backdrop heat flow of well P4 the last day of data sampling.

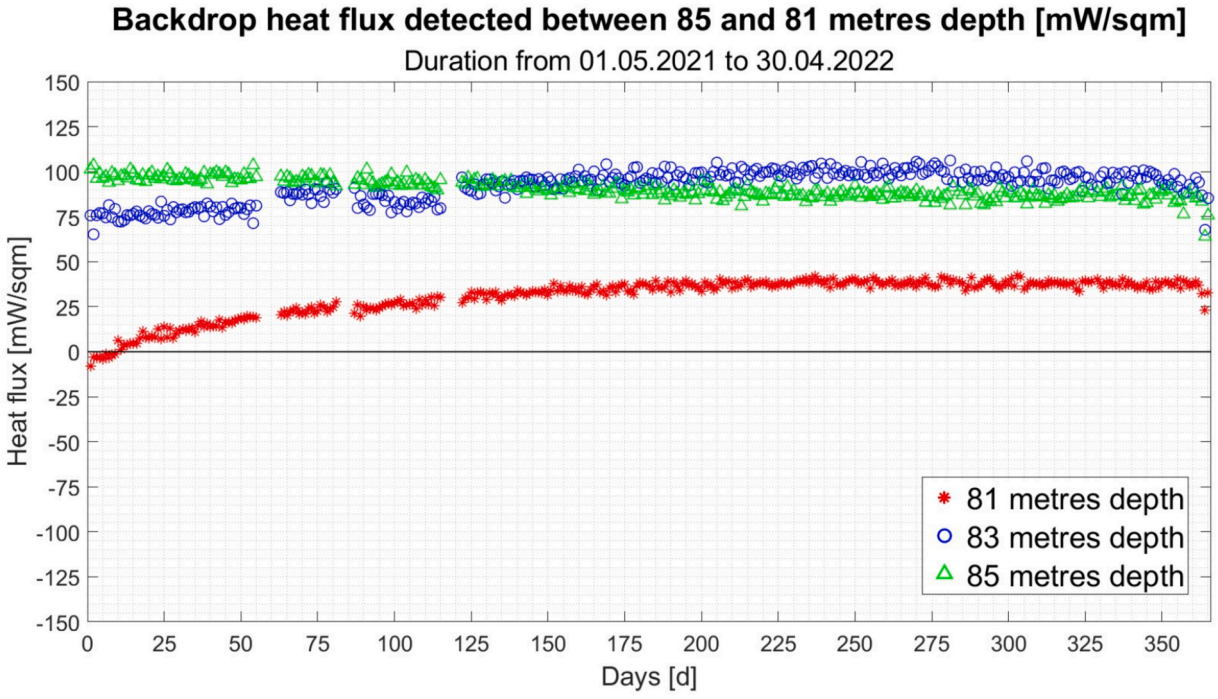

Fig. 16. Backdrop heat flow between 80 and 85 m depth, probe 4.

lithostratigraphic succession of a ground field contains discontinuities, temperature measurements along vertical probes are sufficient to evaluate the geothermal contribution to a BHE.

Depending on the depth, the influence of groundwater flow is not negligible, especially in the middle of the field, where superficial and basal heat transfer phenomena are less relevant. Time evolution of geothermal heat flux rate in deep layers shows changes in direction that are related to this effect.

As the definition of the basal surface boundary conditions of a numerical model significantly affects its final solution, the current study is proposed as reference for design and research purposes in the context of soils similar to the Sabatini stratigraphy. Instead of imposing a constant basal temperature, the definition of an almost constant heat flow at the deepest surface of the geometry is more appropriate to characterize the model of a low-enthalpy geothermal field.

Future outlooks of the current research should focus on the impact of groundwater flow on a BHE field through a more detailed qualitative and quantitative analysis of its contribution and how different

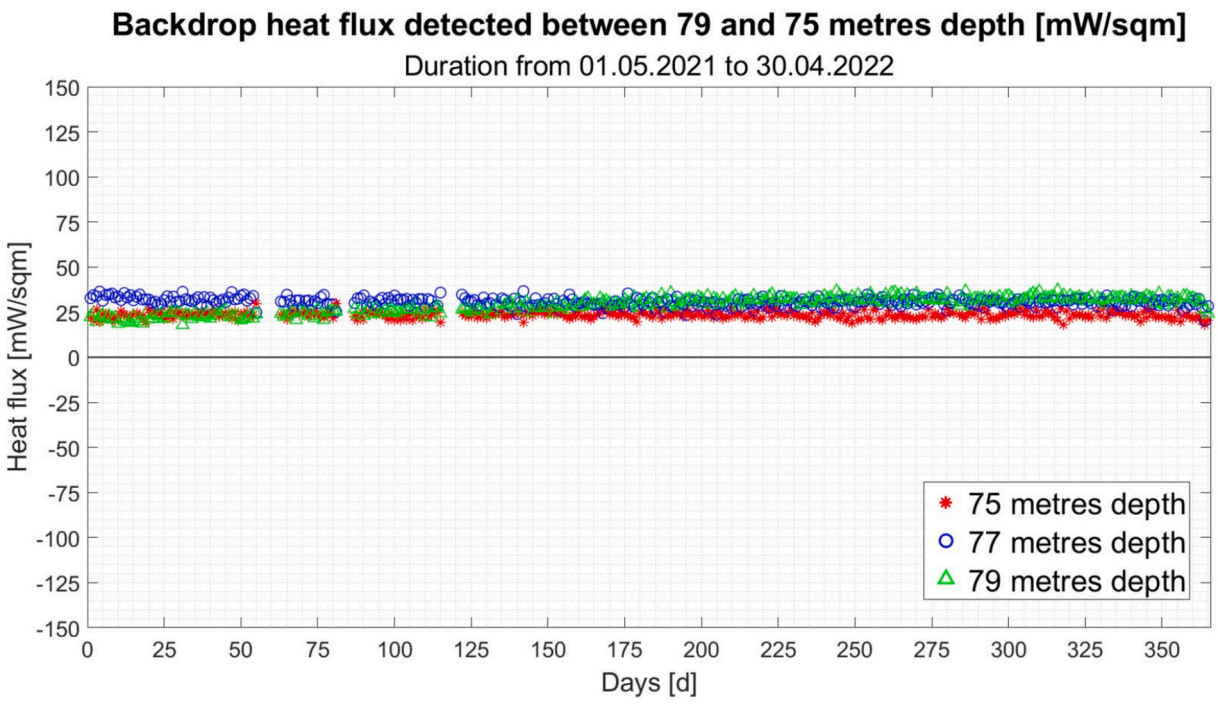

Fig. 17. Backdrop heat flow between 75 and 79 m depth, probe 4.

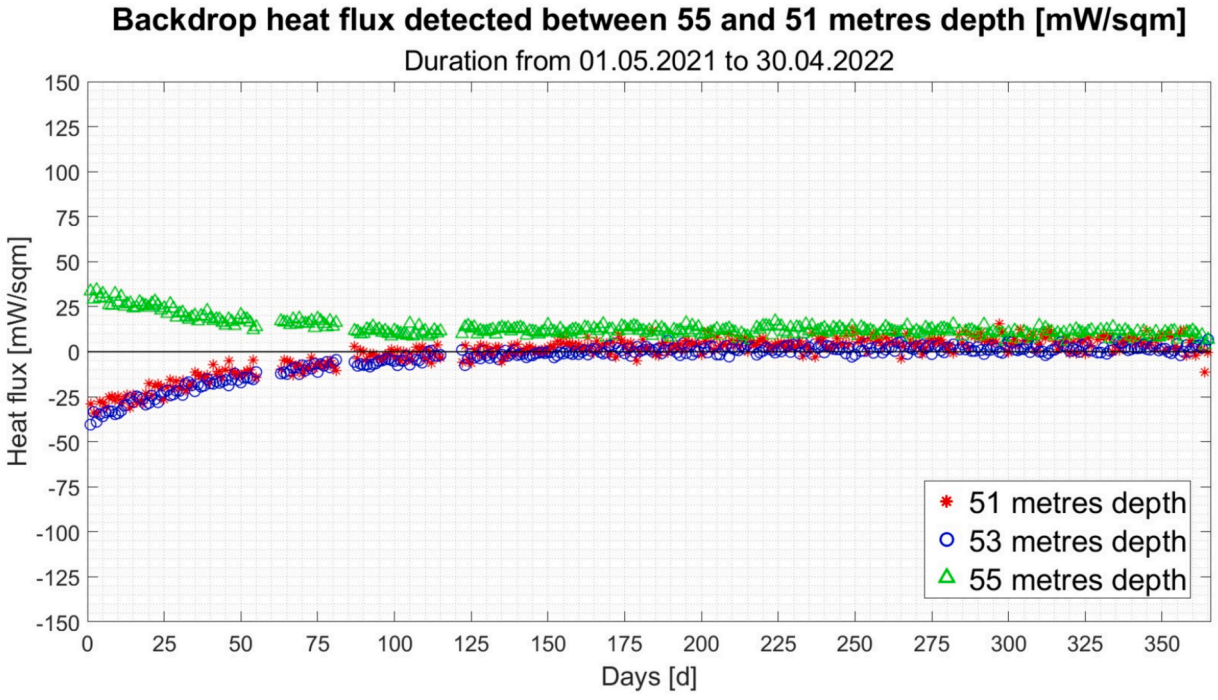

Fig. 18. Backdrop heat flux between 50 and 55 m depth.

lithologies react to the mutual presence of a BHE field and an aquifer. Moreover, the influence of the ground thermal field distribution over depth on the BHE working fluid temperature profile and heat transfer coefficient throughout BHE transient operation should be investigated.

CRediT authorship contribution statement

L. Colacino: Methodology, Investigation, Writing – original draft. **A. C. Violante:** Software, Supervision, Writing – review & editing. **R. Trinchieri:** Funding acquisition. **E. Habib:** Methodology, Supervision, Writing – review & editing.

Declaration of competing interest

The authors declare that they have no known competing financial interests or personal relationships that could have appeared to influence the work reported in this paper.

Acknowledgement

The activity described in this paper is part of the Italian National Electricity System research project funded by the Ministry of Economic Development, MiSE (now renamed as Ministry of Environment and Energy Security, MASE), in two 3-years periods (2019–2021 and 2022–2024). The activity is part of both “Piano Triennale 19-21” and “Piano Triennale 22-24”, regarding the L.A. 1.7 “Tecnologie per la penetrazione efficiente del vettore elettrico negli usi finali”. The research projects are implemented under Programme Agreements between MASE, ENEA, the National Research Council (CNR), Research on the Energy System (RSE S.p.A.), and the main national universities.

Data availability

Data will be made available on request.

References

[1] T. Hermans, F. Nguyen, T. Robert, A. Revil, Geophysical methods for monitoring temperature changes in shallow low enthalpy geothermal systems, Energies 7 (2014) 5083–5118, https://doi.org/10.3390/en7085083.
[2] T. Hermans, S. Wildemeersch, P. Jamin, P. Orban, S. Brouyère, A. Dassargues, F. Nguyen, Quantitative temperature monitoring of a heat tracing experiment using cross-borehole ERT, Geothermics 53 (2015) 14–26, https://doi.org/10.1016/j.geothermics.2014.03.013.
[3] L.C.B. Silva, M.E.V. Segatto, C.E.S. Castellani, Raman scattering-based distributed temperature sensors: a comprehensive literature review over the past 37 years and towards new avenues, Opt. Fiber Technol. 74 (2022) 103091, https://doi.org/10.1016/j.yofte.2022.103091.
[4] J.R. Patterson, M. Cardiff, T. Coleman, H. Wang, K.L. Feigl, J. Akerley, P. Spielman, Geothermal reservoir characterization using distributed temperature sensing at Brady Geothermal Field, Nevada, Lead. Edge 36 (12) (2017), https://doi.org/10.1190/tle36121024a1.1, 1024ª1-1024ª7.
[5] S.J. Ikard, A. Revil, Self-potential monitoring of a thermal pulse advecting through a preferential flow path, J. Hydrogeol. 519 (2014) 34–49, https://doi.org/10.1016/j.jhydrol.2014.07.001.
[6] H. Fuji, H. Okubo, K. Nishi, R. Itoi, K. Ohyama, K. Shibata, An improved thermal response test for U-tube ground heat exchanger based on optical fiber thermometers, Geothermics 38 (2009) 399–406, https://doi.org/10.1016/j.geothermics.2009.06.002.
[7] J. Acuna, P. Mogensen, B. Palm, Distributed thermal response test on a U-pipe borehole heat exchanger, Appl. Energy 109 (2013) 312–320, https://doi.org/10.1016/j.apenergy.2013.01.024.
[8] B. Hainrr, B. Shi, X. Wu, C. Jia, D. Cao, G. Wei, DTS technology for thermal conductivity of ground in Heze, Shangdong province, J. Eng. Geol. 26 (3) (2018) 802–809, https://doi.org/10.13544/j.cnki.jeg.2017-228.
[9] N. Simon, O. Bour, N. Lavenant, G. Porel, B. Nauleau, B. Pouladi, L. Longuevergne, A. Crave, Numerical and experimental validation of the applicability of active DTS Experiments to estimate thermal conductivity and groundwater flux in porous media, Water Resour. Res. 57 (1) (2020), 2020WR028078.
[10] L. del Val, J. Carrera, M. Pool, L. Martinez, C. Casanovas, O. Bour, A. Folch, Heat dissipation test with fiber-optic distributed temperature sensing to estimate groundwater flux, Water Resour. Res. 57 (3) (2021) 2020WR027228.
[11] S.W. Tyler, J.S. Selker, M.B. Hausner, C.E. Hatch, T. Torgersen, C.E. Thodal, S. Schladow, G,, Environmental temperature sensing using Raman spectra DTS fiberoptic methods, Water Resour. Res. 45 (4) (2009) 2008WR007052.
[12] T. Read, O. Bour, V. Bense, T. Le Borgne, P. Goderniaux, M.V. Klepikova, R. Hochreutener, N. Lavenant, V. Boschero, Characterizing groundwater flow and heat transport in fractured rock using fiber-optic distributed temperature sensing, Geophys. Res. Lett. 40 (2013) 2055–2059, https://doi.org/10.1002/grl.50397.
[13] S. Fuchs, N. Balling, A. Mathiesen, Deep basin temperature and heat-flow field in Denmark – New insights from borehole analysis and 3D geothermal modelling, Geothermics 83 (2020) 101722, https://doi.org/10.1016/j.geothermics.2019.101722.
[14] Y. Cherubini, M. Cacace, M. Sheck-Wenderoth, I. Moeck, B. Lewerenz, Controls on the deep thermal field: implications from 3-D numerical simulations for the geothermal research site Groß Schonebeck, Environmental, Earth Sci. 70 (2013) 3619–3642, https://doi.org/10.1007/s12665-013-2519-4.
[15] A. Toth, A. Galsa, J. Madl-Szonyi, Significance of basin asymmetry and regional groundwater flow conditions in preliminary geothermal potential assessment – Implications on extensional geothermal plays, Global Planet. Change 195 (2020) 103344, https://doi.org/10.1016/j.gloplacha.2020.103344.
[16] Y. Wang, Z. Pang, Heat flux in volcanic and geothermal areas: Methods, principles, applications and future directions, Gondw. Res. 122 (2023) 260–278, https://doi.org/10.1016/j.gr.2022.09.010.
[17] V. Pasquale, M. Verdoya, P. Chiozzi, Heat flow and geothermal resources in northern Italy, Renew. Sustain. Energy Rev. 36 (2014) 277–285, https://doi.org/10.1016/j.rser.2014.04.075.
[18] S. Bellani, A. Brogi, A. Lazzarotto, D. Liotta, G. Ranalli, Heat Flow, deep temperatures and extensional structures in the Larderello Geothermal Field (Italy): constraints on geothermal fluid flow, J. Volcanol. Geoth. Res. 132 (2004) 15–29, https://doi.org/10.1016/S0377-0273(03)00418-9.
[19] G. Corrado, S. De Lorenzo, F. Mongelli, A. Tramacere, G. Zito, Surface heat flow density at the Phlegrean fields Caldera (Southern Italy), Geothermics 27 (1998) 469–488, https://doi.org/10.1016/S0375-6505(98)00023-6.
[20] D. Montanari, A. Minissale, M. Doveri, G. Gola, E. Trumpy, A. Santilano, A. Manzella, Geothermal resources within carbonate reservoirs in western Sicily (Italy): a review, Earth Sci. Rev. 169 (2017) 180–201, https://doi.org/10.1016/j.earscirev.2017.04.016.
[21] V.B. Della, F. Lucazeau, V. Pasquale, G. Pellis, M. Verdoya, Heat flow in tectonic provinces crossed by the southern segment of the European Geotraverse, Tectonophysics 224 (1995) 57–74, https://doi.org/10.1016/0040-1951(94)00217-W.
[22] A.C. Violante, M. Proposito, F. Donato, G. Guidi, L.M. Falconi, Preliminary study of a closed loop vertical ground source heat pump system for an experimental pilot plant (Rome, Italy), Renew. Energy 176 (2021) 415–422, https://doi.org/10.1016/j.renene.2021.05.083.
[23] Ukil A. Braendle H., Krippner P., Distributed temperature sensing: Review of technology and applications, IEEE Sensors Journal 12 (2012) 885-892. 1109/JSEN.2011.2162060.
[24] W. Mazzotti, A. Lazzarotto, J. Acuna, B. Palm, Calibration and uncertainty quantification for single-ended raman-based distributed temperature sensing: case study in an 800 m deep Coaxial Borehole Heat Exchanger, Sensors 23 (2023) 5498, https://doi.org/10.3390/s23125498.
[25] G. Bolognini, A. Hartog, Raman-based fibre sensors: trends and applications, Opt. Fiber Technol. 19 (2013) 678–688, https://doi.org/10.1016/j.yofte.2013.08.003.
[26] R. Stierlin, J. Ricka, B. Zysset, R. Bättig, H.P. Weber, T. Binkert, W.J. Borer, Distributed fiber-optic temperature sensor using single photon counting detection, Appl. Opt. 26 (1987) 1368–1370, https://doi.org/10.1364/AO.26.001368.
[27] A.C. Violante, G. Guidi, M. Proposito, S. Mataloni, F. Spaziani, Use of distributed temperature sensing (DTS) coupled to ground source heat exchangers for geological thermo-stratigraphic correlation, Renew. Energy 225 (2024) 120242, https://doi.org/10.1016/j.renene.2024.120242.
[28] E. Urresta, M. Moya, C. Campana, C. Cruz, Ground thermal conductivity estimation using the thermal response test with a horizontal ground heat exchanger, Geothermics 96 (2021) 102213, https://doi.org/10.1016/j.geothermics.2021.102213.
[29] J. Busby, Thermal conductivity and diffusivity estimations for shallow geothermal systems, Q. J. Eng. Geol. Hydrogeol. 49 (2016) 138–146, https://doi.org/10.1144/qjegh2015-079.
[30] Fuchs, et al., Quality-assurance of heat-flow data: the new structure and evaluation scheme of the IHFC Global Heat Flow Database, Tectonophysics 863 (2023) 229976, https://doi.org/10.1016/j.tecto.2023.229976.
[31] K. Pearson, Notes on regression and inheritance in the case of two parents, Proceed. R. Soc. London 58 (1895), 240-242. Doi: 10.1098/rspl.1895.0041.
[32] S. Taviani, H.J. Henriksen, The application of a groundwater/surface-water model to test the vulnerability of Bracciano Lake (near Rome, Italy) to climatic and water-use stresses, Hydrgeol. J. 23 (2015) 1481–1498, https://doi.org/10.1007/s10040-015-1271-0.
[33] 3B Meteo, Archivio Dati Meteo Storici Italiani, https://www.3bmeteo.com/meteo/anguillara/storico, accessed 09/12/2024.
[34] S. Fuchs, A. Forster, B. Norden, Evaluation of the terrestrial heat flow in Germany: a case study for the reassessment of global continental heat-flow data, Earth Sci. Rev. 235 (2022) 104231, https://doi.org/10.1016/j.earscirev.2022.104231.
[35] M. Verdoya, P. Chiozzi, G. Gola, E.E. Jbeily, Conductive heat flow pattern of the central-northern Apennines, Italy, Int. J. Terrestrial Heat Flow Appl. Geothermics 2 (2019) 37–45, https://doi.org/10.31214/ijthfa.v2i1.33.
[36] M. Verdoya, P. Chiozzi, G. Gola, Unravelling the terrestrial heat flow of young orogen: the example of the northern Apennines, Geothermics 90 (2021) 101993, https://doi.org/10.1016/j.geothermics.2020.101993.
[37] C. Pauselli, G. Gola, P. Mancinelli, E. Trumpy, M. Saccone, A. Manzella, G. Ranalli, A new surface heat flow map of the Northern Apennines between latitudes 42.5 and 44.5 N, Geothermics 81 (2019) 39–52, https://doi.org/10.1016/j.geothermics.2019.04.002.
[38] T.M.P. Ratouis, M.J. O'Sullivan, S.A. Alcaraz, J.P. O'Sullivan, The effects of seasonal variations in rainfall and production on the aquifer and surface features of Rotorua geothermal field, Geothermics 69 (2017) 165–188, https://doi.org/10.1016/j.geothermics.2017.05.003.
[39] V.B. Della, S. Bellani, G. Pellis, P. Squarci, Deep temperatures and surface heat flow generation, Anat. Orogen: Apennines Adjacent Mediterranean Basins (2001) 65–76, https://doi.org/10.1007/978-94-015-9829-3_7.
[40] CNR (Centro Nazionale delle Ricerche), Geothopica 2.0 Database, https://geothopica.igg.cnr.it/index.php/it/, accessed 09/12/2024.